



ACADEMIC
PRESS

Available online at www.sciencedirect.com

SCIENCE @ DIRECT®

Journal of Solid State Chemistry 174 (2003) 167–174

JOURNAL OF
SOLID STATE
CHEMISTRY

<http://elsevier.com/locate/jssc>

Structural disorder along the lithium diffusion pathway in cubically stabilized lithium manganese spinel

I. Synchrotron X-ray studies

Nobuo Ishizawa,^{a,*} Douglas du Boulay,^a Masato Hayatsu,^a Satoru Kuze,^a
Yuta Matsushima,^{a,1} Hiromasa Ikuta,^b Masataka Wakihara,^b Yasunori Tabira,^{c,2}
and James R. Hester^d

^a Materials and Structures Laboratory, Tokyo Institute of Technology, 4259 Nagatsuta, Midori Yokohama 226-8503, Japan

^b Department of Chemical Engineering, Tokyo Institute of Technology, 2-12-1 Oookayama, Meguro-ku, Tokyo 156-8552, Japan

^c Research School of Chemistry, Australian National University, Canberra, ACT 0200, Australia

^d Australian Nuclear Science and Technology Organisation, PMB 1, Menai, NSW 2234, Australia

Received 25 July 2002; received in revised form 7 February 2003; accepted 9 April 2003

Abstract

Electron density distribution, EXAFS, and transmission electron microscope studies on stoichiometric $\text{Li}(\text{Mg}_{1/6}\text{Mn}_{11/6})\text{O}_4$ have revealed that: (1) the structure is essentially of spinel-type with slight diffuse scattering, (2) the Li atoms are not all located at the ideal $8a$ site of the $Fd\bar{3}m$ spinel structure, but are partially tetrahedrally distributed along the $8a-16c$ tie line, (3) the O atoms also exhibit a statistical distribution about their ideal positions and (4) the Mn $3d$ electrons are squeezed out toward the open space of the coordinating octahedra with D_{3d} distortion. The present results indicate the possible existence of many metastable Li positions in the structure, suggestive of complicated Li atom hopping routes in conjunction with a local distortion of neighboring atoms at least up to the second shell.

© 2003 Elsevier Inc. All rights reserved.

Keywords: Electron density; Lithium manganese spinel; $\text{Li}(\text{Mg}_{1/6}\text{Mn}_{11/6})\text{O}_4$; Synchrotron X-ray powder diffraction; Lithium diffusion; Structural disorder

1. Introduction

The development of rechargeable lithium ion batteries for electronic devices has stimulated systematic surveys of various candidate materials. Among them the lithium manganese oxides with spinel-type structure have attracted much attention because of their cost-effectiveness, low toxicity and relatively high energy density when used as cathode materials [1–4]. The $\text{Li}_x\text{Mn}_2\text{O}_4$ solid solution with $0 < x < 2$ has a capacity fade problem, but this can be suppressed by partial substitution of Mn with different metal atoms [5–13]. The manganese spinel

crystals partially substituted with Mg are reported to have improved properties for industrial application [13].

In contrast with energetic surveys and extensive studies of new cathode materials, the nature of the Li diffusion in these substances is not well known. The normal spinel structure denoted as AB_2X_4 crystallizes in the $Fd\bar{3}m$ space group; the A atoms are located at the tetrahedrally coordinated $8a$ sites (Wyckoff notation), i.e., $x = y = z = 1/8$, where the origin is taken at the inversion center; the B atoms are located at the octahedrally coordinated $16d$ sites, i.e., $x = y = z = 1/2$; and X atoms are at the tetrahedrally coordinated $32e$ sites, i.e., $x = y = z \approx 0.25$. The high temperature form of LiMn_2O_4 takes this archetypal structure with $A = \text{Li}$, $B = \text{Mn}$ and $X = \text{O}$. The compound undergoes a Jahn–Teller type phase transition near room temperature to a low temperature form with non-cubic symmetry [14–16].

*Corresponding author. Fax: +81-45-924-5360.

E-mail address: nishizaw@n.cc.titech.ac.jp (N. Ishizawa).

¹ Present address: Tokyo University of Agriculture and Technology.

² Present address: Corporate R&D center, Mitsui Mining & Smelting Co., Ltd.

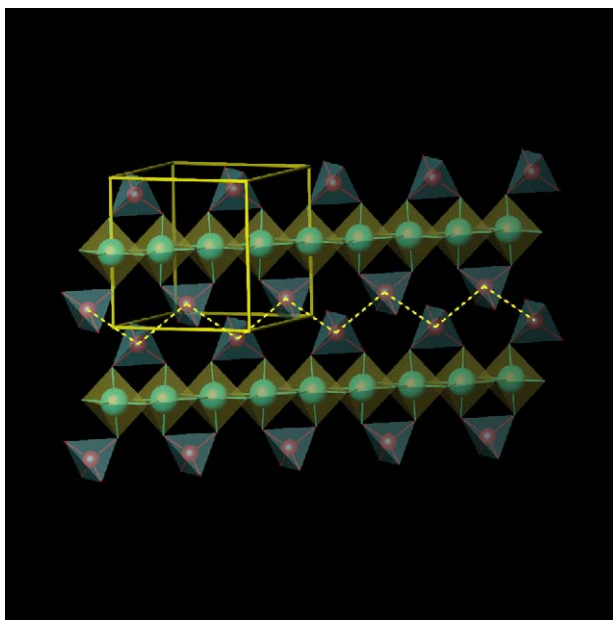


Fig. 1. Connection of lithium tetrahedra and manganese octahedra in the lithium manganese spinel structure sliced parallel to $(\bar{1}10)$. The unit cell is shown as a cube and the Li diffusion pathway as the broken zigzagging line.

The archetypal LiMn_2O_4 spinel structure is composed of MnO_6 octahedra and LiO_4 tetrahedra linked in three dimensions. A slice of the structure parallel to $(\bar{1}10)$ is shown in Fig. 1 to help illustrate the Li diffusion pathway. In this figure there are one-dimensional chains of edge-sharing MnO_6 octahedra running parallel to $[110]$ and to which chains of LiO_4 tetrahedra are attached. These tetrahedra form zigzag chains (highlighted) which intersect the Wyckoff $16c$ octahedral interstices, i.e., at $x = y = z = 0$. The $16c$ site is located at the center of the largest spatial voids in the spinel structure. The conventional understanding of Li diffusion in these materials is that the Li ions hop from the $8a$ to $16c$ sites along the zigzagging chains [17].

It is expected that a flexible local structural distortion accompanies the mobile ion as it migrates through the structure. In LiMn_2O_4 , this should occur for Li typically when it passes through the bottleneck formed by the triangular faces of the LiO_4 tetrahedra. A simple calculation based on the concept of effective ionic radii [18] shows that the bottleneck has an approximate radius of 0.55 Å, slightly smaller than the typical 0.59 Å radii of tetrahedrally coordinated Li cations and significantly smaller than the typical 0.76 Å radii when octahedrally coordinated. The rigidity of the $[\text{Mn}_2\text{O}_4]^{-1}$ framework in the Li diffusion models can thus be questioned, and Amundsen et al. [19] discussed possible local distortions involved. On the other hand, as far as the current authors are aware, no examination has been made of the preferred Li atom positions during

the migration process in lithium manganese spinel. The current study rectifies this omission.

The electron density distribution obtained by X-ray diffraction provides a time and spatially averaged representation of the crystal structure. This information includes details of structural disorder if we look carefully at the residual electron densities obtained from difference Fourier synthesis, and can provide clues for understanding the mobility of ions in the crystal. The present experimental study was thus undertaken to elucidate these points in cubically stabilized lithium manganese spinel, with results and arguments supported thereafter by computational techniques.

The non-stoichiometric nature of the compound designated as $\text{Li}_x\text{Mn}_2\text{O}_4$ is fundamental to its use as a positive electrode material because the Li extraction and insertion take place during the charge and discharge cycles over the lifetime of a battery. However, from the experimental point of view, the non-stoichiometry clouds the interpretation of the observed electron density distribution to some extent. Here a well characterized stoichiometric $\text{Li}(\text{Mg}_{1/6}\text{Mn}_{11/6})\text{O}_4$ compound was chosen for investigation in order to minimize those ambiguities.

The present study of the structural disorder along the Li diffusion pathway in cubically stabilized lithium manganese spinel is the first of two separate papers dealing with: (I) the electron density distribution and (II) molecular dynamics calculation. In the current paper (I), the electron density distribution of cubic $\text{Li}(\text{Mg}_{1/6}\text{Mn}_{11/6})\text{O}_4$ was determined by synchrotron X-ray powder diffraction with new findings about the residual electrons along the Li diffusion pathways and also around O and Mn atoms. The observed disorder of Li and O atom positions are evaluated on the basis of molecular dynamics simulation in the subsequent paper (II).

2. Experimental

2.1. Synthesis

The stoichiometric compounds $\text{LiMg}_{1/6}\text{Mn}_{11/6}\text{O}_4$ were synthesized by solid-state reaction using carbonates, Li_2CO_3 (99.9%, Soekawa Chemical Industries Ltd.), MnCO_3 (99.9%, Soekawa Chemical Industries Ltd.), and $4\text{MgCO}_3 \cdot \text{Mg}(\text{OH})_2 \cdot 3\text{H}_2\text{O}$ (99.9%, Soekawa Chemical Industries Ltd.). The stoichiometric mixture was preheated at 600°C for 6 h, and then heated at 750°C for 3 days in air with several intermediate regrindings followed by slow cooling at a rate of 0.5°C/min. The density of the sample was determined to be 4.19(2) g/cm³ on the basis of a pycnometric study. The value agrees well with the calculated density from the synchrotron X-ray powder diffraction as shown in Table 1. The properties of the sample were detailed by

Table 1
Crystal data and atomic parameters of $\text{Li}(\text{Mg}_{1/6}\text{Mn}_{11/6})\text{O}_4$

a	8.2228(1) Å
V	555.98(1) Å ³
D_x	4.198 g/cm ³
D_m	4.19(2) g/cm ³
SG	$Fd\bar{3}m$
Li	$x = y = z = 1/8$ $U_{11} = 0.012(2)$ Å ² ($U_{11} = U_{22} = U_{33}$, $U_{12} = U_{13} = U_{23} = 0$)
M (Mg, Mn)	$x = y = z = 1/2$ $U_{11} = 0.0054(1)$ Å ² $U_{12} = -0.0008(2)$ Å ² ($U_{11} = U_{22} = U_{33}$, $U_{12} = U_{23} = U_{13}$)
O	$x = y = z = 0.2610(1)$ $U_{11} = 0.0186(4)$ Å ² $U_{12} = -0.0044(7)$ Å ² ($U_{11} = U_{22} = U_{33}$, $U_{12} = U_{13} = U_{23}$)

Hayashi et al. [13]. They also measured the chemical diffusion coefficients of Li in a series of $\text{Li}_x\text{Mg}_{1/6}\text{Mn}_{11/6}\text{O}_4$ with $0 < x < 1$ by the current-pulse relaxation technique, and reported that the values were almost constant at around 10^{-9} cm²/s [13].

2.2. Electron microscopy and EXAFS

Several preliminary experiments were carried out to characterize the crystal quality prior to the X-ray diffraction experiments at room temperature. First, the electron diffraction patterns were recorded using a transmission electron microscope (Philips EM430) to check for the presence of any superstructure reflections or diffuse scattering. The specimens were prepared by crushing and dispersing on holey carbon-coated copper grids. Secondly, an EXAFS study near the Mn K absorption edge was carried out at beamline 14A, Photon Factory, KEK. Powders of MnO, Mn₂O₃ and MnO₂ were also measured for comparison. The crushed powders on adhesive tape were used in a transmission mode. X-rays were monochromated by a Si (111) double crystal monochromator and focused by a toroidal mirror. The EXAFS spectra were obtained in the energy range 6239 through 7743 eV with 4 eV step interval. The dwell time for each step was 10 s for $\text{LiMg}_{1/6}\text{Mn}_{11/6}\text{O}_4$ and 5 s for the others. Ion chambers filled with flowing N₂ gas were used as X-ray detectors. The mean Mn–O distance and the coordination number were calculated from the EXAFS data by the conventional method [20] using a least-squares program [21].

2.3. Synchrotron X-ray powder diffraction

The synchrotron X-ray powder diffraction data were collected at room temperature using the Debye–Scherrer camera at beamline 20B of the Photon Factory, KEK,

Tsukuba [22]. The camera cassette of 573 mm in radius, was loaded with three adjacent image plates to record diffraction patterns and evacuated. The specimen was sealed in a silica glass capillary and rotated during exposure. The intensity data were read and processed by a BAS2000 system [23–24] after exposure. The 0.6047(1) Å wavelength was calibrated using a Si standard powder (NBS 640b).

The least-squares program RIETAN-2000 [25] was used for the Rietveld analysis. The background of the profile was estimated by a spline function and subtracted from the whole diffraction pattern prior to the Rietveld refinement. The peak profile parameters based on a split pseudo-Voigt function [26] and preferred orientation parameters were refined along with the structural parameters. Mg, Mn(III) and Mn(IV) were assumed to statistically occupy the same position. The populations were assumed to be stoichiometric. The parameters converged after several cycles of the least-squares procedure resulting in $R_{\text{WP}} = 9.84\%$, $R_{\text{P}} = 6.70\%$, $R_{\text{F}} = 4.71\%$ and $S = 3.75$. The origin shift was 0.0245(3)° in 2θ . The Caglioti parameters U , V , and W to describe the full-width at half-maximum for the profile became 0.00864(2), 0.00567(1) and 0.002202(1), and the profile asymmetry parameters, A_0 , A_1 and A_2 became 1.03(3), 0.010(8) and $-0.0005(3)$, respectively [25]. Crystal data and final structural parameters are listed in Table 1. The observed and calculated patterns are given in Fig. 2. The calculated interatomic distances are 1.937(1) Å for Li–O and 1.969(1) Å for Mn(Mg)–O.

The difference Fourier map was calculated by the Xtal program package [27]. The structure factor F_h^c of a model structure can be given as

$$F_h^c = \frac{1}{V} \sum_i^{\text{cell}} f_i \exp(2\pi i \mathbf{h} \cdot \mathbf{r}_i), \quad (1)$$

where \mathbf{h} is the scattering vector, \mathbf{r}_i and f_i are the positional vector and the atomic scattering factor of the atom i , and the sum is taken over the unit cell with volume V [28,29]. If we write $F_h^c = |F_h^c| \exp(i\varphi_h^c)$, the electron density distribution $\rho_c(\mathbf{r})$ of the model can be calculated using the Fourier series as

$$\begin{aligned} \rho_c(\mathbf{r}) &= \frac{1}{V} \sum_h F_h^c \exp(-2\pi i \mathbf{h} \cdot \mathbf{r}) \\ &= \frac{1}{V} \sum_h |F_h^c| \exp(-2\pi i \mathbf{h} \cdot \mathbf{r} + i\varphi_h^c). \end{aligned} \quad (2)$$

In a similar way, the experimentally observed electron density $\rho_o(\mathbf{r})$ can be written as

$$\begin{aligned} \rho_o(\mathbf{r}) &= \frac{1}{V} \sum_h F_h^o \exp(-2\pi i \mathbf{h} \cdot \mathbf{r}) \\ &= \frac{1}{V} \sum_h |F_h^o| \exp(-2\pi i \mathbf{h} \cdot \mathbf{r} + i\varphi_h^o). \end{aligned} \quad (3)$$

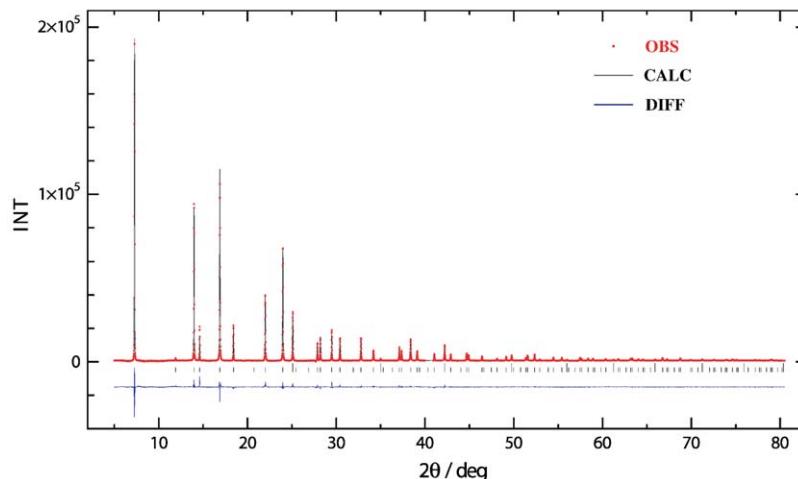


Fig. 2. The observed (cross), calculated and difference (solid lines) synchrotron X-ray powder diffraction profiles for $\text{Li}(\text{Mg}_{1/6}\text{Mn}_{11/6})\text{O}_4$.

If we assume $\varphi_h^o \approx \varphi_h^c$, then the difference electron density $\Delta\rho(\mathbf{r})$ between Eqs. (2) and (3) becomes

$$\begin{aligned} \Delta\rho(\mathbf{r}) &\equiv \rho_o(\mathbf{r}) - \rho_c(\mathbf{r}) \\ &= \frac{1}{V} \sum_h (F_h^o - F_h^c) \exp(-2\pi i \mathbf{h} \cdot \mathbf{r}) \\ &= \frac{1}{V} \sum_h (|F_h^o| - |F_h^c|) \exp(-2\pi i \mathbf{h} \cdot \mathbf{r} + i\varphi). \end{aligned} \quad (4)$$

If an atom i is missing in the model, then $\rho_c(\mathbf{r})$ will be zero around $\mathbf{r} = \mathbf{r}_i$, while $\rho_o(\mathbf{r})$ will show maximum, leading to a peak at that position in the $\Delta\rho(\mathbf{r})$ map. On the other hand, $\Delta\rho(\mathbf{r})$ will be almost zero at the other atom positions in the model because $\rho_o(\mathbf{r})$ is nearly equal to $\rho_c(\mathbf{r})$ around those positions.

An important property of the difference Fourier method is that it is less affected by the series truncation errors [28]. Because the two series Eqs. (2) and (3) converge rapidly at high scattering angle, neglect of the high-order reflections in Eq. (4) has little impact on the Fourier summations. Because of this advantage, the difference Fourier technique is widely used in finding missing light atoms, finding errors in the positional and thermal parameters of atoms in the model, and finding the deformation of the electron density of atoms from the spherical model. In the calculation we assumed a model structure which excludes Li atoms because they were presumed to be distributed in a largely disordered way. Since Li is a much lighter element than O and Mn, our model structure affects to a minimal extent the phase approximation, $\varphi_h^o \approx \varphi_h^c$, while providing the real Li atom distributions without any presupposition.

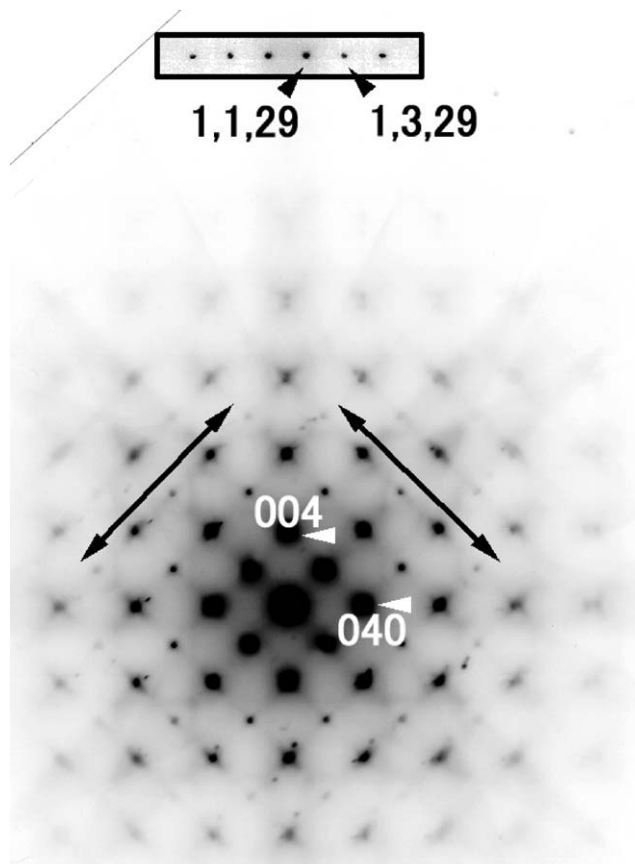


Fig. 3. Diffraction patterns of zero and first layers Laue zones. The arrow indicates the direction of diffuse lines.

3. Results and discussion

A typical $\langle 100 \rangle$ zone axis electron diffraction pattern is shown in Fig. 3. The crystal is essentially of spinel

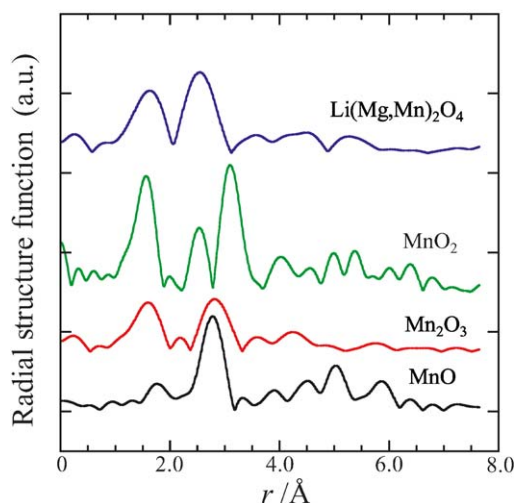


Fig. 4. Radial distribution functions of Mn K EXAFS data for $\text{Li}(\text{Mg}_{1/6}\text{Mn}_{11/6})\text{O}_4$, MnO , Mn_2O_3 and MnO_2 .

type. Neither superstructure reflections nor any signs of the distortion from the spinel face-centered cubic lattice were observed. However, there exists a weak but highly structured diffuse intensity distribution along $\langle 0kk \rangle^*$ directions of the reciprocal space in the zero-order Laue zone. Since sharp Bragg spots are excited in the first-order Laue zone of the same electron diffraction pattern, e.g., the 1,1,29 and 1,3,29 reflections in Fig. 3, the diffuse streaks observed along the $\langle 0kk \rangle^*$ reciprocal lattice vectors are not due to the crystalline quality but indicative of some sort of intrinsic disorder on $\{011\}$ in real space.

The EXAFS analysis of the Mn K absorption edge provides information about the distribution of interatomic distances across all Mn sites throughout the sample. The radial structure functions of the Mn interatomic distances in $\text{LiMg}_{1/6}\text{Mn}_{11/6}\text{O}_4$ spinel and three reference standards, $\text{Mn}(\text{II})\text{O}$, $\text{Mn}(\text{III})_2\text{O}_3$ and $\text{Mn}(\text{IV})\text{O}_2$ are shown in Fig. 4. The profiles of the first and second nearest-neighbor shells in spinel are generally wider than those of the reference materials, indicating a greater distribution of Mn–O and Mn– M ($M = \text{Li}$, Mg and Mn) distances in the spinel. The nearest-neighbor peak position of the spinel is located at a similar radius to the $\text{Mn}(\text{IV})\text{O}_2$ and $\text{Mn}(\text{III})_2\text{O}_3$ standards, while the spinel second nearest-neighbor peak radius matches the smaller component of the $\text{Mn}(\text{IV})\text{O}_2$ second shell split-peak. The mean Mn–O distance and the coordination number of Mn in $\text{LiMg}_{1/6}\text{Mn}_{11/6}\text{O}_4$ was calculated to be 1.926(2) Å and 5.9(4), respectively, with a reliability factor $R = 0.079$. This is consistent with an AB_2X_4 spinel structure containing octahedrally coordinated Mn atoms. In fact Shannon [18] reported octahedral Mn–O bond-lengths of 1.91 and 2.025 Å, respectively for Mn(III) in high spin state and Mn(IV). The mean Mn–O distance observed here falls within that range.

The residual electron density distribution in the $(\bar{1}10)$ plane running through the origin is shown in Fig. 5. Relevant features can be summarized as follows:

- (1) The electron density distribution around the tetrahedral $8a$ site has an asphericity, extending lobes along the directions towards $16c$ octahedral interstices. In addition, a mild peak of electrons exists along the $8a$ – $16c$ tie-line and 0.8–1.5 Å away from $8a$ with a maximum height of approximately $2 e/\text{Å}^3$.
- (2) An accumulation of electrons near the O atoms is also observed. They form peaks at about 0.26 Å apart from the O atom position with maximum height of $3 e/\text{Å}^3$ and oriented along the second-nearest M atom over the tetrahedral void.
- (3) There is an accumulation of electrons around the $16d$ sites occupied by Mn and Mg atoms. They are located about 0.4 Å from M with maximum height of $2 e/\text{Å}^3$ and oriented along the larger space of the MO_6 octahedron with D_{3d} distortion.

The residual electron density distribution along the $8a$ – $16c$ tie-line is shown in Fig. 6. The distribution shows a local minimum at 0.64 Å from $8a$, corresponding to the bottleneck of the LiO_4 tetrahedron. The diffuse peak of electrons in the region between 0.8 and 1.5 Å from $8a$ suggests that some Li atoms have escaped from their tetrahedral LiO_4 cages. The diffuse peak has two maxima at 1.0 and 1.4 Å, which corresponds, respectively, to 0.78 and 0.38 Å from the $16c$ site. The four tetrahedral lobes oriented along $[111]$ vectors

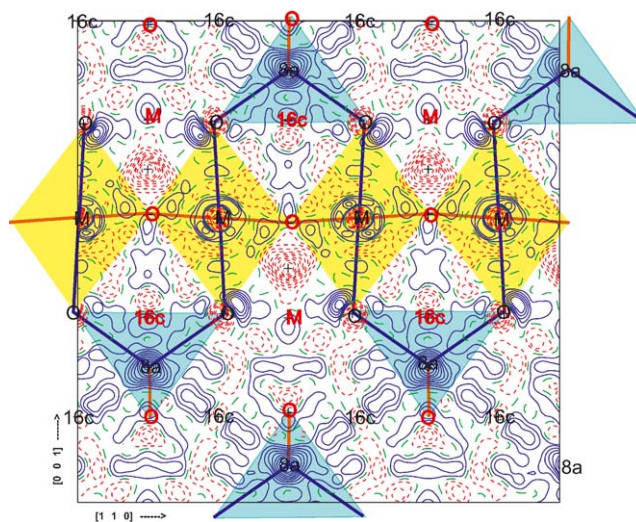


Fig. 5. Difference Fourier map of a 10 Å^2 section parallel to $(\bar{1}10)$ with $0.5 e/\text{Å}^3$ contour intervals. Solid and dashed lines denote positive and negative levels, respectively. The atoms and bonds on the plane are marked in black and those close to but not exactly on the plane in gray. The $8a$ and $16c$ stand for the Wyckoff notations of the ideal Li site and the octahedral interstice, respectively. Projections of MO_6 octahedra and LiO_4 tetrahedra are shown in pale colors.

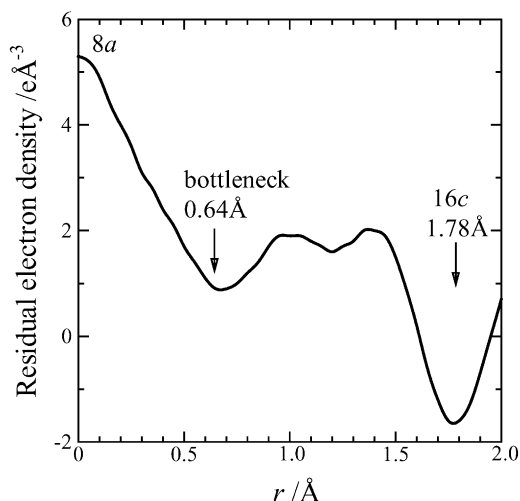


Fig. 6. Changes of residual electron densities along the $8a$ – $16c$ tie-line.

around $8a$ as shown in Fig. 5 were also confirmed by the difference Fourier analysis based on the whole atom model including Li at the ideal $8a$ site. The offset of Li atom positions from $8a$ was estimated to be approximately 0.14 \AA .

It is worth noting that a negative residual electron density of about -1.6 e/\AA^3 is observed on the $16c$ sites. Because this is a difference electron density map this feature implies that the overlap of density attributed to the O atoms in the model exceeds that observed in the experiment at the $16c$ site. We can therefore assume that there are almost no Li atom electrons at $16c$. This agrees with the observations made by Kanno et al. [30] that Li atoms are not located at the octahedral interstices in stoichiometric LiMn_2O_4 .

The weak scattering power of Li for X-rays and various limitations stemming from the powder diffraction experiment does not permit us to apply either anharmonic displacement or split atom models for Li atom distributions in the least-squares refinements with any degree of confidence. Instead, a direct estimation of the probability density function of Li atoms by the molecular dynamics study in Part II supports a model in which Li atoms vibrate almost harmonically at displaced positions.

Although the accumulation of electron density near the O atom sites can also be interpreted as either anharmonic vibrations or static disorder, the latter model is also supported by the molecular dynamics study in Part II. It is noted that the presence of $\langle 0kk \rangle^*$ diffuse streaks in the electron diffraction pattern confirms to the modes of the Li and O atom displacements along $\langle 111 \rangle$ directions on $\{011\}$ planes.

The electron density distribution around Mn can be ascribed to the aspherical distribution of Mn d electrons, squeezed out toward the open spaces of the

MO_6 octahedra to avoid ligands. In order to confirm this, molecular orbital calculations based on first principles were carried out for the Mn(III)O_6 and Mn(IV)O_6 clusters [31–33]. The parameters listed in Table 1 were used to model the clusters with D_{3d} symmetry. The difference electron density was obtained by subtracting the theoretically expected electron density sum of the atomic orbitals of the cluster before self-consistent field (SCF) calculation from that of the molecular orbitals of the cluster after the SCF calculation. The contour maps of the difference electron densities thus calculated around Mn(III) and Mn(IV) in respective Mn(III)O_6 and Mn(IV)O_6 clusters are shown in Fig. 7. They extend six depleted density lobes toward O and positive density lobes toward the open space to avoid the surrounding O atoms. The difference electron density around Mn is essentially the same as that obtained using a larger cluster model of $\text{Li}_9\text{Mn}_{20}\text{O}_{40}$ by Liu et al. [34].

The similar asphericity of the electron density distribution of Mn(III) and Mn(IV) atoms in Fig. 7 originates from our assumption of identical geometries

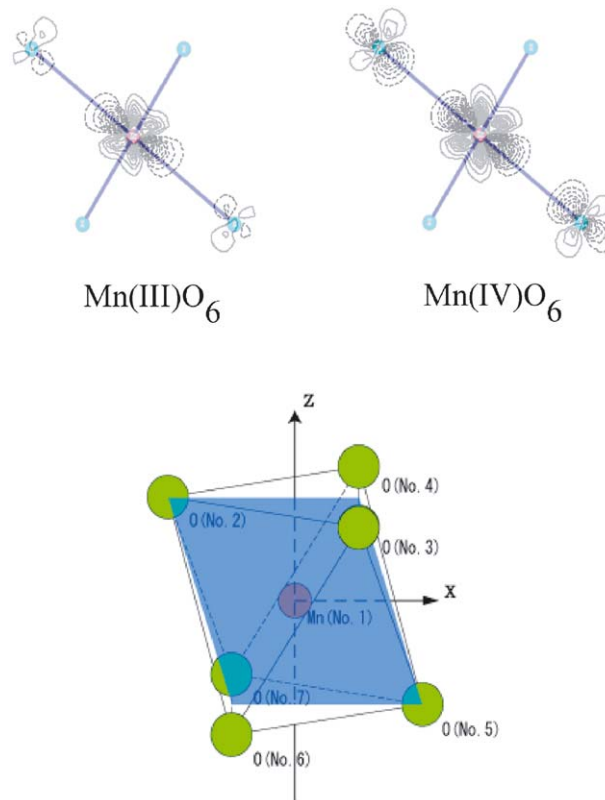


Fig. 7. Theoretically expected difference electron density distribution around Mn(III) (top left) and Mn(IV) (top right) with contour intervals of 0.1 e/\AA^3 , at the section colored in gray of MnO_6 octahedral cluster (bottom). Solid and dashed lines denote positive and negative levels, respectively. The crystallographic three-fold axis was taken as z -axis for the molecular orbital calculation since the cluster has a D_{3d} symmetry.

for both clusters. This assumption may be allowable if we limit our objective to pointing out similarities to the observed residual electron densities of Mn atoms in the difference Fourier map in Fig. 5. However, this assumption is inappropriate if we take into consideration the disorder of O atoms associated with the difference of the bonding nature between Mn(III)–O and Mn(IV)–O. Further analyses on the electron density distribution around Mn atoms require a knowledge of the local symmetries that they possess in their locally deformed surroundings, which is left for future work.

Previous models of Li diffusion in spinel have assumed a simple hopping mechanism utilizing the tetrahedral $8a$ and octahedral $16c$ sites [17]. This simple picture could be replaced with a more elaborate model taking into consideration various stable or metastable Li positions residing along the line connecting $8a$ and $16c$. In addition the disorder of O atom positions presumably plays an important role in the model because the formation of larger openings in the triangular tetrahedral faces by slight shifts of O atom position would facilitate the hopping of Li.

In the structure, each O atom is tetrahedrally surrounded by three M and one Li atom where M stands for Mg(II), Mn(III) or Mn(IV). Depending on the specific combination of the three M s, several off-center displacement modes can be induced for the central O atom. If the oxidation states are exchangeable between nearby Mn atoms, a time-dependent character can be added to the O atom displacements, which in turn affect the Li atom position because the LiO_4 and OLiM_3 tetrahedra interpenetrate each other. Because the Li atom has the smallest oxidation state among the constituent metal atoms, its potential minima may be shallow and more susceptible to the local deformation of the surrounding cluster of atoms, resulting in a dynamical distribution of various positions for Li. This would be a favorable property for Li diffusion in the crystal.

4. Conclusions

Electron density distribution analysis of synchrotron powder X-ray diffraction from stoichiometric $\text{Li}(\text{Mg}_{1/6}\text{Mn}_{11/6})\text{O}_4$ has revealed a disordered distribution of Li and O atoms which were not previously known. The Li atoms are not all located entirely at the ideal tetrahedral $8a$ site of the $Fd\bar{3}m$ spinel structure, but are partially distributed along the line connecting the $8a$ site and the $16c$ octahedral interstice, forming a diffuse peak with maxima at around 0.78 and 0.38 Å from the $16c$ site. The population of Li is negligible at the $16c$ site. The O atoms also exhibit a statistical distribution near their ideal positions, suggesting local disorder depending on the geometrical configuration of the surrounding Li,

Mg, and Mn atoms. The O atom disorder brings distortion to LiO_4 tetrahedra, which in turn aids the Li migration by modifying the size of the triangular face bottlenecks. The present results suggest the existence of several metastable Li positions in the structure with resultant complicated Li atom hopping routes in conjunction with a local distortion of neighboring atoms at least up to the second shell. Any alternation of the oxidation states between Mn(III) and Mn(IV) would attach a time-dependent nature to the local distortion variants, and presumably play a central role in the Li diffusion mechanism.

Acknowledgments

This study was supported by Grant-in-Aid for Scientific Research on Priority Areas (B) (No. 740) from The Ministry of Education, Science, Sports and Culture of Japan. The awards of Australian Research Council post-doctoral fellowship to YT, and the Japan Society of Science for the Promotion of Science Fellowship to DDB are gratefully acknowledged. The synchrotron X-ray powder diffraction was performed at the Australian National Beamline Facility with support from the Australian Synchrotron Research Program, which is funded by the Commonwealth of Australia under the Major National Research Facilities Program. The EXAFS measurement was carried at the Photon Factory, KEK, based on the program 99G190.

References

- [1] J.B. Goodenough, M.M. Thackeray, W.I.F. David, P.G. Bruce, *Rev. Chim. Miner.* 21 (1984) 435–455.
- [2] T. Ohzuku, M. Kitagawa, T. Hirai, *J. Electrochem. Soc.* 137 (3) (1990) 769–774.
- [3] J.M. Tarascon, E. Wang, F.K. Shokoohi, W.R. Mckinnon, S. Colson, *J. Electrochem. Soc.* 138 (10) (1991) 2859–2863.
- [4] D. Guyomard, J.M. Tarascon, *J. Electrochem. Soc.* 138 (10) (1991) 2864–2868.
- [5] R. Bittihn, R. Herr, D. Hoge, *J. Power Sources* 43 (1993) 223–231.
- [6] G. Pistoia, G. Wang, *Solid State Ionics* 66 (1993) 135–142.
- [7] R.J. Gummow, A. de Kock, M.M. Thackeray, *Solid State Ionics* 69 (1994) 59–67.
- [8] G. Li, H. Ikuta, T. Uchida, M. Wakihara, *J. Electrochem. Soc.* 143 (1) (1996) 178–182.
- [9] F. Le Cras, D. Bloch, M. Anne, P. Strobel, *Solid State Ionics* 89 (1996) 203–213.
- [10] A.D. Robertson, S.H. Lu, W.F. Averill, W.F. Howard Jr., *J. Electrochem. Soc.* 144 (10) (1997) 3500–3504.
- [11] A.D. Robertson, S.H. Lu, W.F. Howard Jr., *J. Electrochem. Soc.* 144 (10) (1997) 3505–3512.
- [12] D. Song, H. Ikuta, T. Uchida, M. Wakihara, *Solid State Ionics* 117 (1-2) (1999) 151–156.
- [13] N. Hayashi, H. Ikuta, M. Wakihara, *J. Electrochem. Soc.* 146 (4) (1999) 1351–1354.
- [14] A. Yamada, M. Tanaka, *Mater. Res. Bull.* 30 (6) (1995) 715–721.

- [15] K. Oikawa, T. Kamiyama, F. Izumi, B.C. Chakoumakos, H. Ikuta, M. Wakihara, J. Li, Y. Matsui, *Solid State Ionics* 109 (1998) 35–41.
- [16] J. Rodríguez-Carvajal, G. Rousse, C. Masquelier, M. Hervieu, *Phys. Rev. Lett.* 81 (21) (1998) 4660–4663.
- [17] M. Wakihara, *Mater. Sci. Eng. R* 33 (2001) 109–134.
- [18] R.D. Shannon, *Acta Crystallogr. A* 32 (1976) 751–767.
- [19] B. Ammundsen, J. Roziere, M.S. Islam, *J. Phys. Chem. B* 101 (1997) 8163–8165.
- [20] B.K. Teo, P.A. Lee, *J. Am. Chem. Soc.* 101 (1979) 2815–2832.
- [21] Y. Udagawa, X-sen kyushubisaikouzou (in Japanese), Gakkai-Shuppan center, Japan, 1993, pp. 176–218.
- [22] T.M. Sabine, B.J. Kennedy, R.F. Garrett, G.J. Foran, D.J. Cookson, *J. Appl. Crystallogr.* 28 (1995) 513–517.
- [23] BAS2000: FUJIX BAS2000 Phosphorimaging System Operation Manual, Fuji Film Co., 1989.
- [24] J. Miyahara, K. Takahashi, Y. Amemiya, N. Kamiya, Y. Satow, *Nucl. Instrum. Methods A* 246 (1986) 572–578.
- [25] F. Izumi, T. Ikeda, *Mater. Sci. Forum* 321–324 (2000) 198–203.
- [26] H. Toraya, *J. Appl. Crystallogr.* 23 (1990) 485–491.
- [27] S.R. Hall, D.J. du Boulay, R. Olthof-Hazekamp (Eds.), *Xtal 3.7*, University of Western Australia, Web address: <http://Xtal.crystal.uwa.edu.au/>, 2000.
- [28] D. Viterbo, in: C. Giacovazzo (Ed.), *Fundamentals of Crystallography*. IUCr, Oxford, 1992, pp. 366–367.
- [29] *International Tables for X-ray Crystallography*, Vol. IV, IUCr, Kynoch Press, England, 1974, pp. 99–101.
- [30] R. Kanno, M. Yonemura, T. Kohigashi, Y. Kawamoto, M. Tabuchi, T. Kamiyama, *J. Power Sources* 97–98 (2001) 423–426.
- [31] H. Adachi, M. Tsukada, C. Satoko, *J. Phys. Soc. Jpn.* 45 (3) (1978) 875–883.
- [32] F.W. Averill, D.E. Ellis, *J. Chem. Phys.* 59 (1973) 6412–6418.
- [33] D.E. Ellis, H. Adachi, F.W. Averill, *Surf. Sci.* 58 (1976) 497–510.
- [34] Y. Liu, T. Fujiwara, H. Yukawa, M. Moronaga, *Solid State Ionics* 126 (1999) 209–218.